Elipot, Shane; Hughes, Chris; Olhede, Sofia; Toole, John. 2013 Coherence of western boundary pressure at the RAPID WAVE array: boundary wave adjustments or deep western boundary current advection? *Journal of Physical Oceanography*, 43 (4). 744-765. 10.1175/JPO-D-12-067.1

Coherence of Western Boundary Pressure at the RAPID WAVE Array: Boundary Wave Adjustments or Deep Western Boundary Current Advection?

SHANE ELIPOT AND CHRIS HUGHES

National Oceanography Centre, Liverpool, United Kingdom

SOFIA OLHEDE

University College London, London, United Kingdom

JOHN TOOLE

Woods Hole Oceanographic Institution, Woods Hole, Massachusetts

(Manuscript received 2 April 2012, in final form 20 December 2012)

ABSTRACT

This study investigates the coherence between ocean bottom pressure signals at the Rapid Climate Change programme (RAPID) West Atlantic Variability Experiment (WAVE) array on the western North Atlantic continental slope, including the Woods Hole Oceanographic Institution Line W. Highly coherent pressure signals propagate southwestward along the slope, at speeds in excess of 128 m s^{-1}, consistent with expectations of barotropic Kelvin-like waves. Coherent signals are also evidenced in the smaller pressure differences relative to 1000-m depth, which are expected to be associated with depth-dependent basinwide meridional transport variations or an overturning circulation. These signals are coherent and almost in phase for all time scales from 3.6 years down to 3 months. Coherence is still seen at shorter time scales for which group delay estimates are consistent with a propagation speed of about 1 m s^{-1} over 990 km of continental slope but with large error bounds on the speed. This is roughly consistent with expectations for propagation of coastally trapped waves, though somewhat slower than expected. A comparison with both Eulerian currents and Lagrangian float measurements shows that the coherence is inconsistent with a propagation of signals by advection, except possibly on time scales longer than 6 months.

1. Introduction

Under a changing climate, it is of crucial importance to identify the processes by which adjustments of the Atlantic meridional overturning circulation (MOC) take place in the real ocean. As atmospheric forcings vary, MOC anomalies at high latitudes triggered by changes in deep-water formation travel equatorward along the western boundary as coastally trapped waves, leaving in their wake altered circulations and meridional transports (Johnson and Marshall 2002). Eventually, anomalies should also be distributed by advective means, either by the Deep Western Boundary Current (DWBC) or via interior routes, as partly evidenced by numerical simulations (Zhang 2010), Lagrangian observations (Bower et al. 2009), or water mass diagnostics (Peña-Molino et al. 2011). Simultaneous observations of MOC variability as a function of time and latitude are lacking to verify these theoretical expectations, derived for idealized or approximated oceanic configurations. Furthermore, the real ocean presents intricate topography, continuous stratification, and horizontal circulations, which complicate this simple picture.

This paper investigates the relationships between observations of pressure at three mooring lines on the continental slope of the western North Atlantic (Fig. 1), part of the Rapid Climate Change programme (RAPID) West Atlantic Variability Experiment (WAVE). The underlying motivations for these observations are that boundary pressures are in theory proportional to zonally integrated meridional transports, while boundary pressure gradients are proportional to the vertical shear, or overturning component of those transports (Hughes et al.

Corresponding author address: Shane Elipot, National Oceanographic Centre, Joseph Proudman Building, 6 Brownlow Street, Liverpool, L35DA, United Kingdom.
E-mail: shane.elipot@noc.ac.uk

DOI: 10.1175/JPO-D-12-067.1

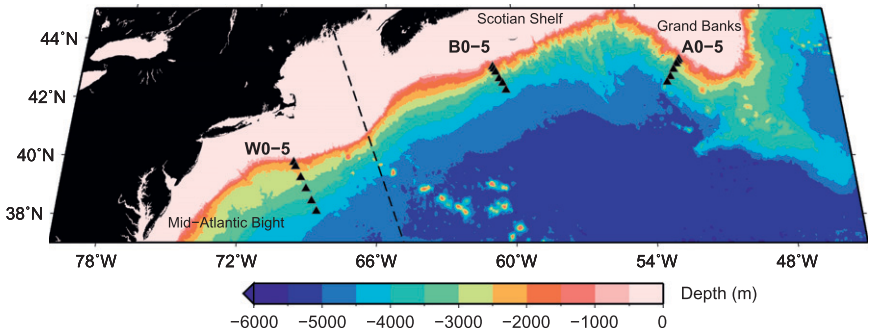

FIG. 1. Western North Atlantic bathymetry and locations of moorings at RAPID WAVE Line A (A0–A5) and Line B (B0–B5), and moorings at Woods Hole Line W (moorings are called here W0–W5 for convenience). The dashed line indicates the topographic section for which we report the results of O'Rourke (2009) of baroclinic wave structure calculation. Bathymetry data are from Smith and Sandwell (1997) topography database version 13.1.

2013). Bingham and Hughes (2008) showed in an ocean global circulation model (OGCM) how the boundary pressure and directly zonally integrated transports time series are related in a way that is consistent with the zonally integrated geostrophic zonal momentum balance. We use here observations of boundary pressure time series to test the hypothesis that the western boundary communicates pressure anomalies. This mechanism has been put forward in numerical studies to explain the meridional coherence of the MOC (Roussenov et al. 2008).

This paper is organized as follows. Section 2 contains a short review of the concept of bottom pressure on eastern and western boundaries as a measure of zonally integrated meridional transport across an ocean basin and provides the motivation for this study. The same section then exposes briefly the theoretical expectations for boundary waves applicable to our observations. Section 3 describes the relevant data from RAPID WAVE used to analyze boundary pressures and pressure gradients. Section 4 describes the methods employed to derive the pressure gradient time series at two mooring lines. Section 5 presents the results of correlation, coherence, and delay estimations of pressure and pressure gradient time series and compares the results to expectations. Section 6 provides a summary and the concluding remarks.

2. Theoretical considerations and expectations

a. *Meridional transport and western boundary pressure*

Integrating horizontally across an ocean basin section the zonal geostrophic momentum balance $\rho f v = \partial p/\partial x$ (where ρ is the in situ density, f the Coriolis frequency, and v the meridional velocity) shows that the meridional mass transport per unit depth $M(z) = \int_{x_W}^{x_E} \rho v \, dx$ is the difference between the bottom pressure at depth z on the eastern slope at longitude $x_E(z)$ and the bottom pressure on the western slope at $x_W(z)$:

$$fM(z) = -p_W(z) + p_E(z). \tag{1}$$

As will be seen from the data presented in section 3, much of the pressure variability is independent of depth on the slope. But an overturning circulation must by definition change direction with depth and hence involves pressure anomalies that vary with depth. To focus on the overturning component of the transport, we consider the vertical derivative of (1):

$$f\frac{\partial M(z)}{\partial z} = -\frac{\partial p_W(z)}{\partial z} + \frac{\partial p_E(z)}{\partial z}, \tag{2}$$

which relates the vertical shear of the mass transport $\partial M/\partial z$ to two boundary pressure gradient terms; the first term $-(\partial p_W/\partial z)/f$ defines the western boundary contribution to the overturning transport, and the second term $(\partial p_E/\partial z)/f$ the eastern boundary contribution. See Hughes et al. (2013) for a comprehensive discussion of this formulation.

An immediate question is which of these two terms, which can be estimated independently, is more important for variability in the zonal integral. Using 19 years of OGCM data, Bingham and Hughes (2008) showed that interannual variability in volume transport between 100 and 1300 m at 42°N in the Atlantic Ocean could be calculated from (1) using only bottom pressure from the western boundary with a skill of 92%.[1] In the deeper layer between 1300 and 3000 m the skill reached 96%.

[1] The skill of a variable y to represent another variable x is $1 - \sigma^2(x - y)/\sigma^2(x)$, where $\sigma^2(x)$ is the variance of x.

Thus, the eastern boundary plays very little role in interannual variability within the model. The relative importance of each boundary has been studied from observations of the 26°N RAPID MOC array by Kanzow et al. (2010). They showed that the western boundary dominated the total variance [2.0 Sv (1 Sv $\equiv 10^6$ m^3 s^{-1}) versus 1.3 Sv rms amplitude of the variations], despite the control of the annual cycle by the eastern boundary (Chidichimo et al. 2010). We focus here on the western boundary variability, which is expected to reflect first the propagation of disturbances from high to low latitudes.

b. Connectivity of transports

At multiannual time scales, advection of water masses at depth by the fast DWBC and by the slower so-called interior pathways eventually carry density anomalies and modify zonally integrated transport between boundaries (e.g., van Sebille et al. 2011). At relatively shorter time scales—in a matter of months—the meridional coherence of transports is expected to be achieved by the propagation of disturbances in the pressure and velocity fields carried by subinertial boundary waves. All such waves propagate cyclonically around the ocean basin (Huthnance 1978) and hence carry signals southward along the western boundary. Model studies (Bingham et al. 2007) suggest that some signals propagate rapidly from north to south, but there is a significant decoupling between subpolar and subtropical MOC variability at interannual to decadal periods. We provide here a short review of the theories and present some specific expectations for our region of study.

1) THEORIES OF BOUNDARY WAVES

The combination of the effects of topography, stratification, and planetary vorticity produces a wide variety of wave modes in the ocean (Rhines 1970). At the continental slope neglecting the β effect in comparison with the steep topography, Huthnance (1978) showed that this resulted in an infinite, discrete sequence of coastally trapped waves (CTW). In the extreme case of a stratified ocean with a steep sidewall spanning much less than a baroclinic Rossby radius of deformation in the horizontal, these waves are a series of Kelvin waves as found in the study of Johnson and Marshall (2002). The other extreme, of sloping topography and no stratification, leads to topographic Rossby waves (TRW) (Wang and Mooers 1976). In all cases in the Northern Hemisphere, the phase of these waves propagates with the shallow topography to their right, and in the long wave limit the group velocity is in the same direction. These are therefore the wave modes that we would expect to communicate pressure changes resulting from high-latitude processes to lower latitudes, along the western boundary.

2) O'ROURKE (2009)'S CALCULATIONS FOR REALISTIC CONDITIONS

For our purpose, we will consider and report here some relevant results from the wave study of O'Rourke (2009) who specifically examined the possible characteristics of Kelvin-like waves and CTW on the western boundary of the North Atlantic, for long wavelength waves (i.e., in the limit of frequency $\ll f$, appropriate for most of the signals we are considering here). She calculated the structure of the pressure field of waves and their along slope speeds at a number of discrete topographic profiles extracted from the General Bathymetric Chart of the Oceans (GEBCO) dataset (British Oceanography Data Centre 2003) between 28° and 43°N. She solved numerically the continental shelf wave vorticity equation for the free surface barotropic cases, and she used the BIGLOAD2 program of Brink and Chapman (1985) for the baroclinic cases, with an offshore density profile calculated from the temperature-salinity climatology of Lozier et al. (1995).

O'Rourke (2009)'s study produced propagation speeds for the gravest mode for the barotropic case in the range 170–220 m s^{-1} for the region. This wave mode 0 is effectively a deep ocean barotropic Kelvin wave mode (Wright and Xu 2004) and would not be greatly affected by the presence of stratification, as in the real ocean. The natural length scale for these waves, perpendicular to isobaths, is the barotropic Rossby radius ($\sqrt{gH}/f$), which is about 2000 km here. These wave modes have very little structure over the width of the continental slope, and therefore should produce a western boundary pressure signal which is almost independent of bathymetry and depth.

For the higher modes including stratification, because of the complexity of the real topography, the BIGLOAD2 program did not return a consistent picture of CTW modes at different positions along the boundary between 28° and 43°N. Nonetheless, we present as an example her results for a carefully examined topographic section centered at 40.5°N, which is highlighted in Fig. 1. This section is typical of the wide shelf configuration found in our study region, and should provide a useful point of comparison for the delays estimated between the transport time series based on pressure gradients derived in section 4. The pressure structure of the first 3 baroclinic wave modes and their associated wave speeds are shown in Fig. 2. Mode 1 with one zero crossing of the pressure along the slope is not a pure coastal baroclinic Kelvin wave but a wave modified by the sloping topography and stratification, with isolines of pressures tilted over a horizontal length scale comparable to the slope itself. With a first baroclinic Rossby

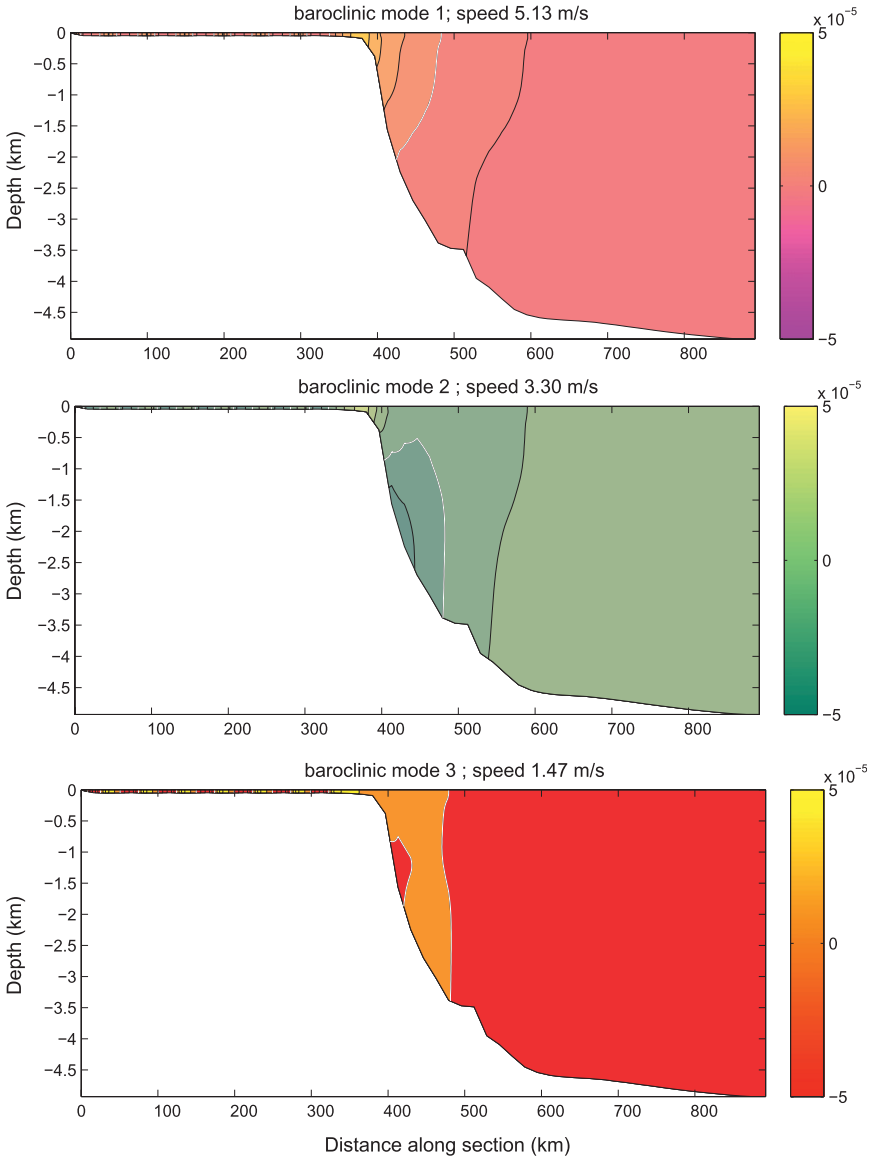

FIG. 2. Coastally trapped wave solution modes (top to bottom) 1, 2, and 3 for the baroclinic (stratified) case for the topographic profile centered on 40.5°N (dashed line in Fig. 1). The free-wave form of the solutions is $\Psi(x, y, z, t) = \phi(x, z)e^{(ky-\omega t)}$, where x is the coordinate or distance along the section, y the coordinate along the continental slope, z the depth coordinate, k the wavenumber in the y direction, ω the radian frequency, and t is the time variable. The solutions $\phi(x, z)$ are presented for pressure, with arbitrary scaling for each panel. Zero contours are drawn in white. The corresponding wave speed ω/k is indicated above each panel. Adapted from O'Rourke (2009).

radius Ro in this region of about 20 km (Chelton et al. 1998), the expected scaling for the tilt of nodal lines of $NH/fL = 1$ leads to a horizontal displacement of the nodal line between bottom and top of the ocean of about πRo $\approx$ 60 km, which is a good match for the displacements we see. The speed of this wave at this section is 5.13 m s^{-1}, which is approximately a lower limit for all other speeds that O'Rourke (2009) diagnosed between 28° and 43°N for this mode. This first baroclinic mode is somewhat faster than the $O(1)$ m s^{-1} value usually found for the baroclinic Kelvin wave seen in an idealized two-layer vertical sidewall basin (Johnson and Marshall 2002). Modes 2 and 3, with respectively two and three zero crossings in bottom pressure, have more complicated structures for the pressure field along the slope than for the wave mode 1. These do not have the vertical nodal

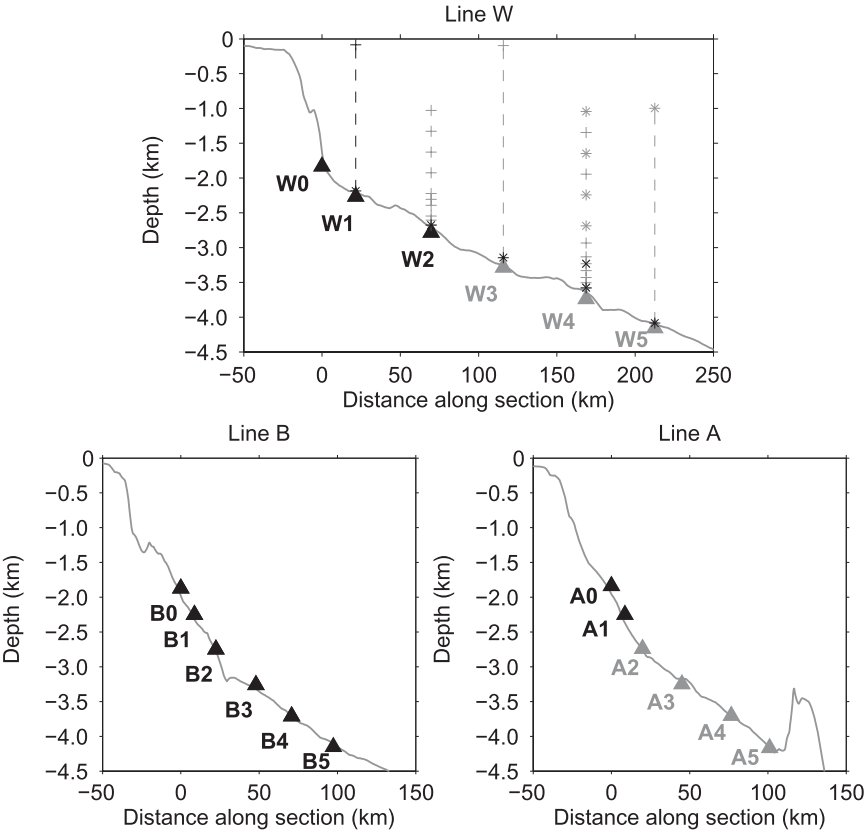

FIG. 3. Vertical sections along (top) WHOI Line W and (bottom) (left) Line B and (right) Line A in their 2004 instrumental configuration. At Line W, the vertical-dashed lines are moorings equipped with McLane profilers. Plus symbols are temperature and salinity measuring instruments. Cross symbols are direct velocity measuring instruments. The instruments on moorings used to derive bottom pressure gradients are plotted in black. The rest of the instruments in gray are used to estimate the transport across the array as in Toole et al. (2011). The black triangles are bottom pressure recorders (BPRs) used in this study as deployed in 2004. The gray triangles are BPR records that were not used in this study (They were either not recovered or did not return usable data). At Lines B and A, not all BPR records are available for the period 2004–08. At Line A, the BPR with gray symbols were not recovered.

contours of barotropic mode, or the horizontal nodes of pure baroclinic Kelvin waves, but are truly hybrid modes, showing a degree of bottom trapping (Huthnance 1978). They have here relatively slower wave speeds at 3.30 m s^{-1} for mode 2 and 1.47 m s^{-1} for mode 3.

3. Data

a. RAPID WAVE deployment and recovery cruises

Investigators of the U.K. National Oceanography Centre (NOC) deployed an observational array called RAPID WAVE since April 2004 (Fig. 1) as part of the wider U.K. Rapid Climate Change programme. The WAVE array originally consisted of three measurement lines spanning the continental slope: Lines A and B were instrumented by NOC, which also supplemented additional instruments along Woods Hole Oceanographic Institution (WHOI) Line W (Toole et al. 2011) (Fig. 3). Lines A and B originally included six lander bottom pressure recorders (BPRs) each, which were deployed during the RSS *Charles Darwin* cruise 160 in August 2004. During the RSS *Discovery* cruise 308 in July–August 2006 only BPRs A0, A1, B0, B1, B2, and B3 were recovered. In view of the BPR losses, Line A was abandoned and six BPRs at Line B (B0 to B5) were redeployed. In October 2007 during the CCGS *Hudson* expedition 2007–045 the BPRs B2, B3, B4, and B5 were recovered and redeployed. In September–October 2008 during the CCGS *Hudson* expedition 2008–037 these BPRs were all recovered except B1. At that time Line B was

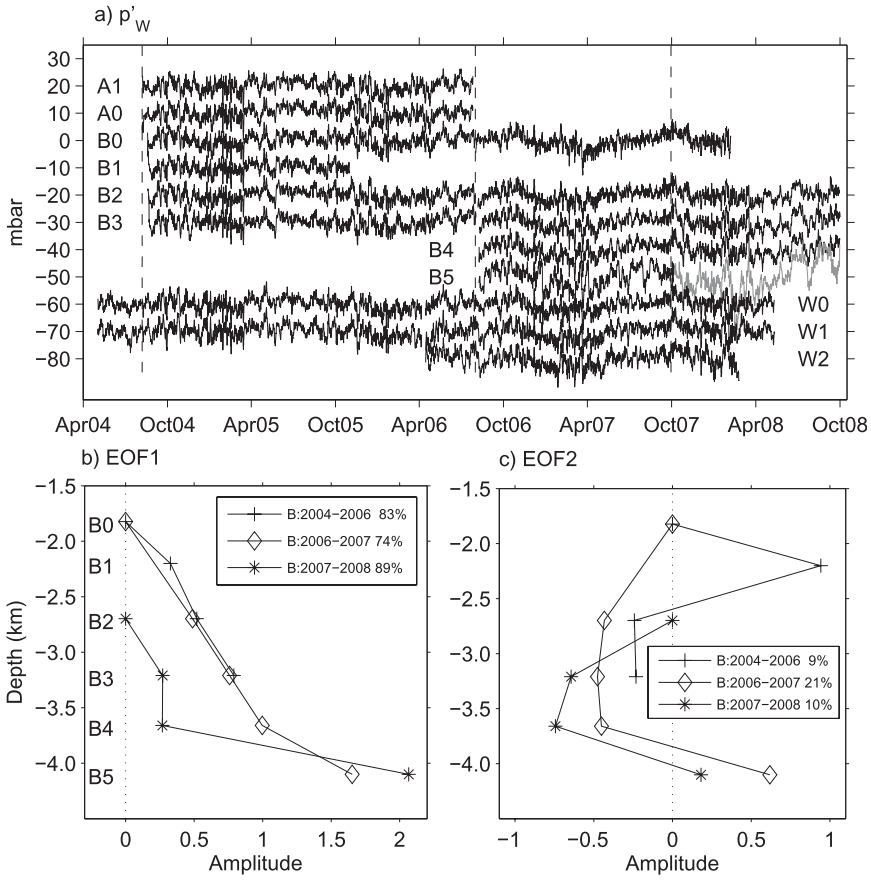

FIG. 4. (a) Western boundary pressure anomalies at Line A moorings A0 and A1, Line W moorings W0 to W2, and Line B moorings B0 to B5. The second recovered deployment at B5 plotted in gray exhibits larger variability at low frequencies and was not used for this study. The time series are low-pass filtered to retain periods longer than one day for this plot. (b) EOF1 and (c) EOF2 of Line B boundary pressure records minus the shallowest records (with a zero EOF amplitude by construction) for the three deployment periods 2004–06, 2006–07, and 2007–08. The legend in each panel indicates the percentage of variance explained by the modes for each time period. For comparison purposes, the EOF1 amplitude in (b) was scaled to align their slopes between the depths of B2 and B3.

replaced by the RAPID–Scotian Line in collaboration with the Canadian Bedford Institute of Oceanography (Hughes et al. 2013), but the data from this new line are not used here.

At Line W, the WAVE operations for 2004–08 took place during five cruises: six BPRs were deployed (W0 to W5) during the R/V *Oceanus* cruise 401 in 2004; only two BPRs were recovered (W0, W1) and the others lost, and three were redeployed (W0, W1, W2) during the R/V *Oceanus* cruise 421 in April 2006; two of these three BPRs (W0, W1) were recovered and three redeployed (W0, W1, W5) during the R/V *Oceanus* cruise 446 in May 2008; and W4 was recovered and W3 was deployed during the R/V *Endeavor* cruise 454 in September 2008. Eventually, the W2 BPR was recovered during the 2010 R/V *Atlantis* cruise 17 but its record extended only into 2008.

b. Bottom pressure recorder processing

Only a usable subset of the quality controlled and processed 15-min interval BPR records of the WAVE array are considered for this study (Fig. 4). Unfortunately, electronics problems resulted in some of the earlier deployments producing sporadic false data but rarely lasting more than a few hours at a time. False points were identified by comparison with an average of neighboring points in time (after subtraction of tides fit to the good points, thus requiring some iteration). Gaps shorter than one day were filled by a combination of linear interpolation of tidal residual plus short period variability taken from a neighboring good record from the same line. Spectra of the resulting time series and of differences between neighboring records (not shown)

revealed that pressure differences contain a factor of 100 less power than the total pressure, in a band between the inertial period and about 5 days. The noisy records, after replacement of bad points, generally showed similar difference spectra at periods longer than about 2.5 days, suggesting that the editing procedure was acceptable at these periods. Nonetheless, the records from the 2006 deployments at B0 and B2 remain noticeably noisier than others. Finally, an exponential-linear trend with time (Watts and Kontoyiannis 1990) was also removed from each record, typically with a range of a few tens of mbar or less (in one case reaching a range of 109 mbar).

c. *Selected WHOI Line W velocity and density records*

Woods Hole Line W spans the continental slope from 38° to 40°N, roughly perpendicular to isobaths (Figs. 1 and 3). Details about deployment history and instruments can be found in Toole et al. (2011). To derive the pressure gradient down the slope at Line W (see section 4), data from near-bottom fixed instruments were used. The data from the McLane Moored Profiler (MMP) on mooring W1 were also used to obtain an estimate of near-bottom density and velocity at two depth levels, 1000 and 1788 m (Fig. 3). This last depth level corresponds to the depth of an additional short mooring holding a BPR, called here W0, deployed originally in 2004 as part of WAVE. All the velocity and temperature–salinity near-bottom instruments used returned good data with three exceptions. At mooring W1 the near-bottom current meter failed from 6 December 2004 incurring a gap in the record until 30 April 2005. At mooring W4, the near-bottom Acoustic Doppler Current Profiler located 111 m above bottom failed for the 2004–06 deployment so that an estimate of the near-bottom velocity was taken from the Vector Averaging Current Meter (VACM) 452 m above the bottom instead. The MMP on W1 failed between mid-April 2006 and early April 2007 and synthesized data for this time period were created similarly to Toole et al. (2011), based on regressions between the data from MMPs at this site for the other time periods, and the data of the fixed sensors at the top and bottom of W1. The high-sampling-rate fixed instrument data records were low-pass filtered to retain frequencies less than 1 cycle per day (cpd) and then sampled every 12 h. The MMP at W1 was programmed to burst sample every fifth day a set of 4 one-way profiles, which are averaged here to reduce inertial and tidal oscillations. The 5-day interval times series were then interpolated linearly every 12 h for consistency with the other time series. The resulting near-bottom velocity and density records are shown in Fig. 5. Note that the data from the rest of the Line W instruments are also used here to derive the volume transport within the trapezoidal region formed by the array (see section 4).

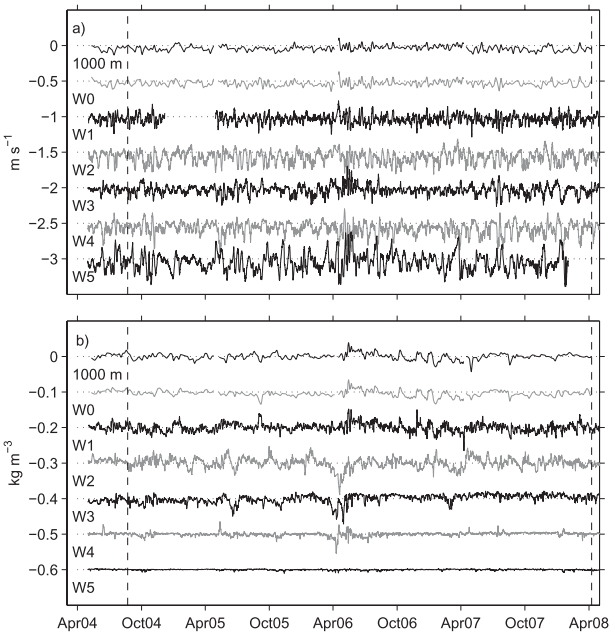

FIG. 5. Records at WHOI Line W of (a) along slope velocity and (b) in situ density anomalies at 1000 m and the depth of W0 (1788 m) from the McLane profiler at W1 and from near-bottom current meters at moorings W1 to W5. For plotting purposes, the time series at W1 to W5 were low-pass filtered to retain periods longer than 1 day.

4. Methods

In this section we explain the methods that were implemented to derive at Line W and at Line B the western boundary pressure gradient time series and their associated integrated form as western boundary transports below and relative, which is referenced, to 1000 m.

a. *Calculating pressure differences at Line W*

One of the two methods of Hughes et al. (2013) is used to derive the western boundary pressure gradient $\partial p_W/\partial z$ at Line W, relative to 1000 m. The methods allow us to reconstruct boundary pressure gradients from near-bottom measurements of density and velocity along a continental slope. The result is a drift-free estimate of pressure gradient, which could not be obtained otherwise by multiple deployments of BPRs at large depths because of instrumental drift (Watts and Kontoyiannis 1990). First, as in Hughes et al. (2013), the applicability of the method chosen at Line W is tested at intra-annual time scales.

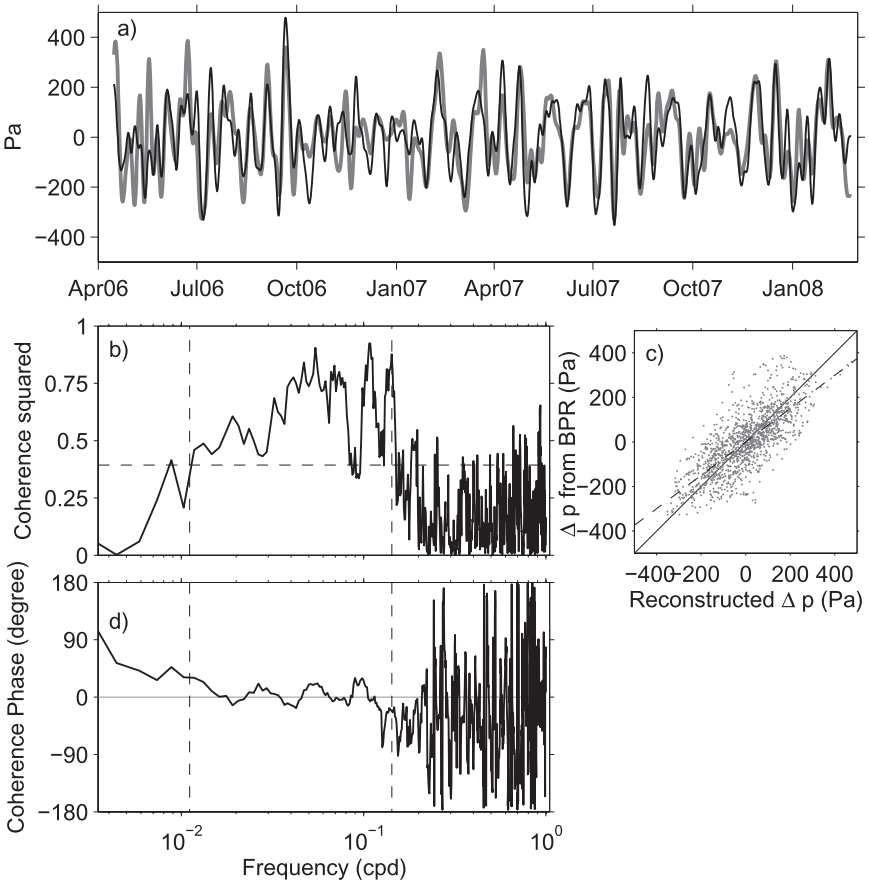

FIG. 6. Analysis of bottom pressure difference Δp between moorings W2 and W1: (a) from BPR data (black line) and reconstruction from density and velocity (gray line). Both time series are bandpass filtered to retain frequencies between $^1/_{90}$ and $^1/_7$ cpd indicated by vertical dashed lines in (b),(d). (b) Coherence squared and (d) coherence phase between the BPRs pressure difference and the reconstructed pressure difference. In (b), the horizontal-dashed line indicates the 95% confidence level for coherence squared (the significant level is valid at any fixed frequency). (c) Scatterplots of the filtered reconstructed pressure differences (y axis) and pressure differences from BPR data (x axis) at 12-h intervals; the dashed lines are the least squares fits to the scatter points (slope 0.74); for comparison, the solid black lines is the slope 1, intercept 0 curve.

The method we use is a generalization of the hydrostatic equation along a sloping bottom assuming that the flow is steered by topography. The three-dimensional oceanic pressure gradient is $\nabla p = -\mathbf{k} \times (\rho f \mathbf{u}_g) - \mathbf{k}\rho g$, with $\mathbf{u}_g$ the geostrophic velocity, g the acceleration of gravity, and $\mathbf{k}$ the upward vertical unit vector. With the z-axis positive upward, the vertical component of the differential of the bottom pressure on the sea floor defined by $z = -H$, along a three-dimensional path of horizontal component $ds = -dz/H$ where $H_s = \partial H/\partial s$, is

$$\delta p_b = -\left(\frac{\rho f u_L}{H_s} + \rho g\right)\delta z, \qquad (3)$$

where u_L is the horizontal geostrophic velocity to the left of the horizontal component of the path (traversed in the direction from shallow toward deep water so that δz is negative). To test the method, first the left-hand side of (3) is computed from 22 months (April 2006 to February 2008) of detided and detrended pressure records from BPRs deployed at the bases of moorings W1 (2242-m depth, two deployments over this period) and W2 (2752-m depth, one deployment), which are separated horizontally by 48.2 km and vertically by 510 m (Fig. 3). Second, the right-hand side of (3) is computed with averages of velocity and density anomalies from instruments located 116 m above the bottom at W1 and 75 m above bottom at W2.

Cross-spectral analysis (see the appendix for the method employed) between the two time series (Figs. 6b,d) shows that, for periods between about 7 and 90 days, the pressure reconstruction explains typically more than

50% of the variance, reaching 92% in some frequency bands, and is approximately in phase with the pressure difference from BPRs. The coherence squared decreases dramatically for periods shorter than 7 days, as it is possible that ageostrophic motions start to dominate at these time scales. The coherence squared becomes not significant at periods longer than 90 days, and this is likely ascribable to the detrending of the BPR records affecting their spectra more severely toward low frequencies (for reference, a relatively large linear trend of 76 mbar or 7600 Pa over this nearly 2-yr period has been subtracted from the W2 record). To quantify the quality of the reconstruction we therefore bandpass filter the time series to retain frequencies between 1/90 and 1/7 cpd, as shown in Fig. 6a. The regression coefficient of the reconstruction onto the BPR pressure difference is 0.74 (scatterplot in Fig. 6c), and therefore the amount of the total variance explained by the reconstruction is only 57%. The rms difference is 0.97 mbar, which translates to a volume transport error of 1.05 Sv per km of depth [according to (2) with $f = 0.92 \times 10^{-4}$ s^{-1} and a reference density of 1000 kg m^{-3} (Hughes et al. 2013)]. This error, if sustained over 3120 m of depth, gives an error estimate for the transport of 3.2 Sv. This error is comparable with the expected natural variability of transports (Cunningham et al. 2007) and significantly larger than the error obtained using the more favorable geometry of the RAPID–Scotian Line (Hughes et al. 2013). Nonetheless, we will see that the correlation between the two pressure-derived time series obtained for this study (see section 5) is an a posteriori validation of their usefulness for studying the propagation of signals along the boundary.

For the purpose of estimating $\partial p_W/\partial z$, the right-hand side of (3) is applied in six discrete steps from 1000 to 4120 m down the continental slope at 12-h interval from 11 May 2004 to 8 April 2008. Following the methodology of Hughes et al. (2013), the values used for ρ in (3) are the in situ density anomalies with respect to the mean density profile as we are not interested in the mean hydrostatic pressure here. Other referencings of pressure could be used but this only affects the mean values, irrelevant for our subsequent analyses which are based on temporal anomalies. A mean pressure at each step also arises from the mean velocity but once again it is not relevant for our analysis and is ignored here. In contrast to the test above, the time series of reconstructed pressure differences were only low-pass filtered below 1 cpd, therefore retaining variability on long time scales, including interannual, which would not be accessible otherwise from BPR data. The first two steps, from 1000 m to W0 (1788 m), and then to the base of mooring W1 were computed by approximating the velocity and density at these depths along the slope by the data collected by the MMP on mooring W1, actually located offshore of the slope (the horizontal distance at 1000 m depth between W1 and the slope is 32 km; see Fig. 3). When the near-bottom velocity record was missing at W1, the velocity there was taken equal to the velocity from the MMP at the depth of W0 for the W0–W1 step, and equal to the velocity from W2 for the W1–W2 step.

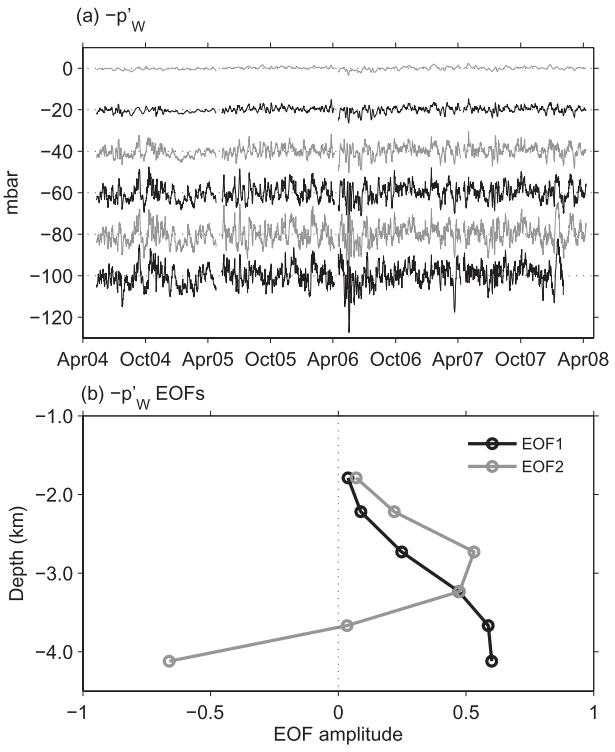

FIG. 7. Western boundary bottom pressure analysis at Line W. (a) Time series of western pressure anomalies $-p'_W$ at the depths corresponding to the base of mooring W0 (top curve) to W5 (bottom curve), subsequently offset by 20 mbar. Black and gray colors are alternated for legibility. One mbar is equivalent to a zonally integrated northward volume transport of 1.08 Sv km^{-1} of depth at this latitude. (b) First two EOF patterns of the pressure anomaly time series in (a) presented as a function of depth. The first mode explains 81.3% of the variance and the second mode 11.3%.

The three gaps occurring in the pressure time series (maximum length 15.5 days) because of mooring turnovers were filled by replacing values (initially zero) by a lowpass-filtered version of the time series and iterating (less than 30 times) until the rms difference between iterations was less than 0.1 Pa. The data records at W5 stop about 4 months before the other records, and the pressure time series there was filled by using a linear regression model based on all preceding pressure data (explaining 72% of the variance at W5). The time series of pressure anomalies $-p'_W(z)$, proportional to northward transports according to (1), are shown in Fig. 7a for the six depth steps.

b. Vertical structure of the pressure variability on the slope

We analyze the vertical structure of the boundary pressure variability. At Line W, the first empirical orthogonal function (EOF) of the boundary pressure $-p'_W(z)$ time series (Fig. 7c), which explains 81.3% of the variance, is a monotonic function, increasing in amplitude with depth. The second EOF explaining only 11% of the variance shows a kink below 3500 m with a reversal of sign. At Line B we also examine the vertical structure of the pressure variability by calculating the first two EOFs for three deployment periods (2004–06, 2006–07, and 2007–08) after low-passing the time series to retain time scales longer than one day. To focus on the variability of pressure differences—or pressure gradient—we subtract from all records the shallowest record available before computing the EOFs. The results for the first two EOFs in each case are plotted in Fig. 4. The sum of the first two modes explains between 92% and 99% of the variance. Similar structures to Line W are found as follows: the first EOFs are single signed increasing with depth while the second EOFs exhibit sharp reversals of sign below 3500 m. Only the second EOF for the 2004–06 deployment is very different but this one is calculated without data below 3700 m. The greater variability at both lines below 3700 m approximately can be associated with bottom-trapped TRW activity, which has been extensively observed and described in this region (e.g., Thompson and Luyten 1976; Louis et al. 1982), or we speculate to the increasing eddy activity occurring over the Abysal Plain to the south and east. Despite the bottom-intensified variability, the EOF analyses at both lines suggest strongly that the part of the pressure gradient that is a near-linear function of depth is likely to capture a coherent mode of variability across the RAPID WAVE array. Since through the 2004–08 period we always have at least two records available at any time shallower than 3500 m we can achieve at Line B an estimate of the boundary pressure gradient between 1000 m and 4000 m by a linear approximation as explained next.

c. Calculation of transports

1) LINE W

The pressure-derived volume transport time series anomaly T_W is computed as

$$T_W = \int_{-4120}^{-1000} \frac{-p'_W(z)}{\rho_0 f} dz. \quad (4)$$

Practically a trapezoidal integration is conducted in the six discrete intervals between 1000 m and W5 at 4120 m. The resulting transport is the western boundary end-point contribution to the zonally integrated meridional transport below and relative to 1000-m depth. This time series is shown in Fig. 8 to put it in the context of the DWBC at Line W. The standard deviation of T_W is 6.5 Sv but note that the uncertainty from the pressure reconstruction is at about 3.2 Sv and thus only 24% of the signal variance. In one noticeable event lasting less than 4 days centered on 18 May 2006, T_W reached an anomaly of −37.3 Sv, associated with large anomalies of near-bottom velocity and density from W1 to W4 (Fig. 5). However this corresponds to the period when the MMP at W1 had failed and for which the data at W0 and 1000 m were estimated from the fixed instruments on W1: as such this event may be overestimated because of errors in the procedure used to fill missing data.

2) LINE B

The longest overlapping time period of single BPR deployments at Line B is 708 days (Fig. 4), a time scale that should therefore be seen as an upper limit of reliable time scales in these records. At each time step, a least squares fit to $p_W(t, z) = a(t) + b(t)z$ was conducted to give a time series of $b(t) = \partial p_W/\partial z$. To account for apparent increased noise in two records from the 2006 deployment, B2 was downweighted by a factor of 2 in the fit for this period, and B0 was downweighted initially by a factor of 2, increasing to a factor or 3 in 2007. B5 is a record clearly associated with variability below 3500 m (EOF2 in Fig. 4c) distinct from the near-linear pressure gradient above (EOF1). Thus we ignored B5 in the fit to be consistent with time periods when B5 is absent. Gaps in the time series $b(t)$, between deployments, were filled by replacing values in the gaps (initially zero) by a low-pass-filtered version of the time series (periods > 5 days), and iterating six times.

The time series $b(t)$ filtered to retain periods longer than one day is shown in Fig. 9. It is a pressure gradient time series in units of pressure per unit depth (left axis), and also converted to a pressure-derived volume transport time series T_B (right axis) between $z_1 = 1000$ m and $z_2 = 4000$ m by

$$T_B = \int_{z_2}^{z_1} \left(\int_{z_2}^{z_1} -\frac{1}{\rho f} \frac{\partial p_W}{\partial z} dz \right) dz = \frac{b}{2f\rho_0} \Delta z^2,$$

with $\Delta z = z_2 - z_1 = 3000$ m, $f = 9.853 \times 10^{-5}$ s^{-1}, and $\rho_0 = 1040$ kg m^{-3}. This integration assumes that the transport per unit depth at 1000 m is a constant in time, chosen here as zero as this corresponds approximately to the zero crossing of the MOC upper cell. Like the time series T_W derived previously T_B is a western boundary contribution to the meridional transport anomaly below

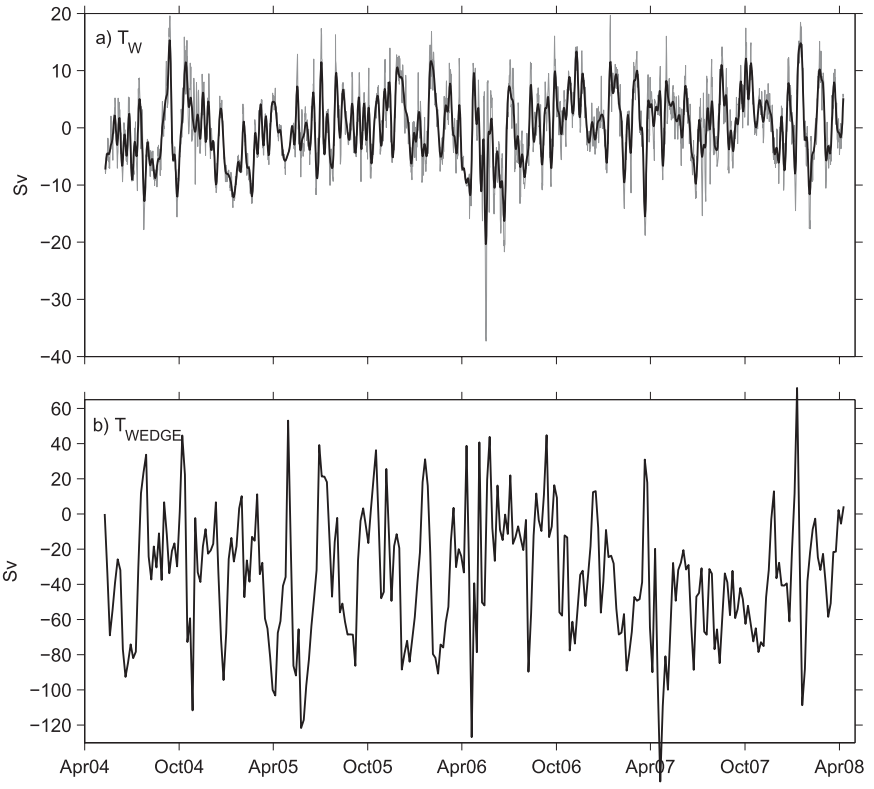

FIG. 8. (a) The T_W western overturning transport time series between 1000 and 4120 m, relative to 1000 m. The gray line is the 12-h step time series and the black line is the 10-day low-passed version. (b) The T_{WEDGE} volume transport at Line W below 1000 m between the continental slope to the west and mooring W5 to the east (see Fig. 3). Note the different scales between (a) and (b).

and relative to 1000 m. The effect of choosing a different reference depth for T_B is to rescale the amplitudes of the variability while retaining the temporal structure. The standard deviation of T_B is 5.1 Sv, which is comparable within error bars to the standard deviation of T_W (6.5 Sv), which is a transport computed for the same depth layer.

d. Relationship between zonally integrated and DWBC transports at Line W

As an aside, it is interesting to consider the relationship between T_W and the transport of the DWBC. From Line W data, Toole et al. (2011) estimated the DWBC transport as the sum of four density-layer transports of Upper Labrador Sea Water, Classical Labrador Sea Water, Iceland–Scotland Overflow Water, and Denmark Strait Overflow Water. Each layer transport was defined at each time step as the maximum of the streamfunction computed from the westernmost mooring (W1) to the easternmost mooring (W5), in bins separated horizontally by the middistance points between moorings. Potential biases when the streamfunctions did not reach their maxima within the array were also assessed. Here, T_W is significantly anticorrelated (-0.28) with Toole et al. (2011)'s DWBC transport. Yet, we find it more appropriate to compare T_W in detail to the transport within the fixed "wedge" region below 1000 m formed by the continental slope to the west and W5 mooring to the east, thereafter called T_{WEDGE}, plotted in Fig. 8b. Here, T_{WEDGE} is evidently correlated (at 0.85) with the DWBC transport as calculated in density layers (not shown) by Toole et al. (2011).

Here, T_W was low-pass filtered below 10 days and subsampled every 5 days for comparison to T_{WEDGE}. The zero-lag correlation between these two time series is then -0.14, which is statistically significant only at the 94% confidence level following the methodology of Ebisuzaki (1997) for serially correlated time series. The clear result is that the DWBC shows much more variability than the zonally integrated measure T_W and is only weakly, negatively, correlated with it. Given that both measures involve the current measurements, a degree of correlation is to be expected. The fact that it is a negative correlation, though surprising, is also to be

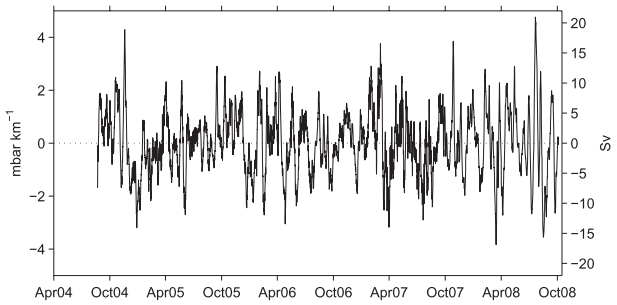

FIG. 9. Time series of western pressure gradient $\partial p_W/\partial z$ at Line B (mbar km^{-1}) (left axis); the right axis is labeled in equivalent transport unit (Sv) since the pressure gradient is integrated to obtain the layer transport T_B in the 1000–4000-m-depth range as $(\Delta z)^2\partial p_W/\partial z/(2f\rho_0)$ with $\Delta z = 3000$ m, $f = 9.826 \times 10^{-5}$ s^{-1}, and $\rho_0 = 1040$ kg m^{-3} (see text).

expected. Combining (2) and (3) along a sloping western boundary gives

$$f\frac{\partial M_W}{\partial z} = -\frac{\partial p_W}{\partial z} = g\rho_W + \left(\frac{\rho f v}{\partial H/\partial x}\right)_W. \qquad (5)$$

In the Northern Hemisphere at the western boundary where $\partial H/\partial x > 0$, at constant density, (5) predicts that the transport shear is of the same sign as the near-bottom meridional geostrophic velocity. A northward velocity will induce a positive shear in the transport so that the zonally integrated flow becomes more southward with increasing depth along the slope, which is counterintuitive.

As an illustration of how this can come about, consider the illustration shown in Fig. 10, which is similar to synoptic observations of across-line velocity at Line W based on ship surveys (Fig. 2 in Toole et al. 2011) but rather different from the Eulerian mean velocity observed by the array (Fig. 3 in Toole et al. 2011). A barotropic (in the sense uniform in the vertical) boundary current is flowing southward over a western boundary with a velocity anomaly $-c < 0$, while to the east a barotropic current of opposite sign flows over flat topography with longitudinal extent δ. To put this situation in the context of the North Atlantic MOC we require that the net area-integrated meridional transport to be zero but this is not necessary for our purpose—only that no changes occur to the shear because of the region to the east. Setting the uniform velocity to the east to $c/(2\delta)$ can achieve both conditions. The resulting volume transport anomaly per unit depth $Q(z)$ varies linearly with depth, from $-c/2$ at the surface to $c/2$ at the bottom. This illustrates how a southward velocity anomaly of a barotropic DWBC leads to a northward anomaly of the integrated transport below a reference depth because of the changing width of the basin.

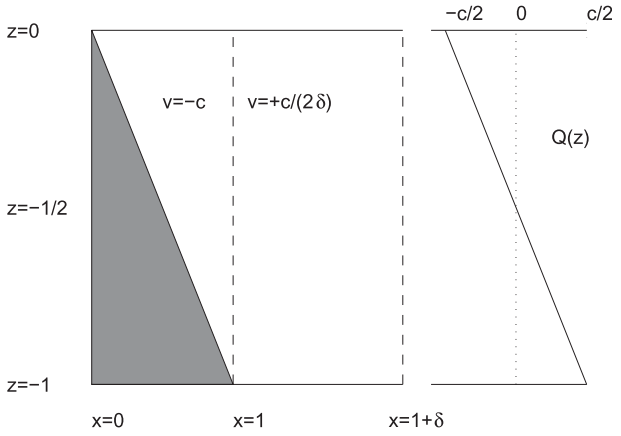

FIG. 10. (left) Schematic of an idealized configuration of barotropic overturning. A current with uniform meridional velocity $v = -c$ flows over a continental slope (gray shading), which occupies the west part of the domain from $x = 0$ to $x = 1$ and between $z = 0$ and $z = -1$. A barotropic current with velocity $v = +c/(2\delta)$ of opposite sign flows over a flat bottom in the east part of the domain from $x = 1$ to $x = 1 + \delta$. (right) Depth profile of the corresponding volume transport per unit depth $Q(z)$.

Directly measured transport of the DWBC on one hand, either in depth space, or in density space such as in Toole et al. (2011), and a integral quantity like T_W on the other hand, are two conceptually different ways of thinking about meridional transport and the MOC in the North Atlantic (see e.g., Hughes et al. 2013). As an example, T_W provides no detailed information on water mass variability, which directly measured transports can (Peña-Molino et al. 2011).

5. Results on correlation, coherence, and group delay

We first investigate the relationships between the bottom pressure time series from lines A, B, and W (Fig. 4a) between 2004 and 2008. Then we investigate the relationship between the integrated pressure gradient time series at lines B and W.

a. Pressure time series: Fast barotropic waves propagation

The pressure records are strongly correlated all across the WAVE array. For the two periods of overlapping single deployments delineated by vertical dashed lines in Fig. 4a, the strongest correlation (0.96) is found between B3 and B4 for the 2006–07 period, and the weakest correlation (0.61) is found for the same time period between W2 and B5. Close examinations of the time series reveal that various short time delays exist between all time series. Cross-spectral analyses (not shown) show that the coherence squared is close to one for subinertial

frequencies but decreases at superinertial frequencies, and also toward the zero frequency. The lack of coherence at low frequencies is partly ascribable to the various instrumental drifts and the unique corrections applied to each record.

Group delays between all BPR records were estimated for two time periods: August 2004 to August 2006 and August 2006 to October 2007. Within each interval, the longest overlapping period between BPR pairs was used. The details of the signal processing method are given in the appendix, but conceptually the method consists of estimating the derivative of the phase of the cross spectra with respect to frequency, which is the group delay (Hannan and Thomson 1973). The method allows for selection of the frequency range over which to conduct the procedure, and estimation of delays that are not necessarily an integer multiple of the time step of the time series and possibly shorter. In contrast, conventional lagged-correlation methods integrate over all frequencies irrespective of the signal-to-noise level and can only provide estimates that are multiples of the time step. The range of frequencies over which the estimation is conducted is chosen here to correspond to subinertial frequencies, where the coherence is the largest.

The group delay estimates (Fig. 11) are not formally statistically different from zero according to 95% confidence intervals based on two standard deviations of the formal distribution of the estimates (see appendix). Despite this, a general pattern emerges with 25 delays out of the 28 estimated indicating that pressure signals propagate equatorward along the boundary from lines A to B to W. Three delays only indicate signals propagating northward, with one corresponding to an unphysical speed and extracted from one of the noisiest records. Within each line, signals are found to propagate either upslope or downslope with no consistent direction. With approximate distances between the lines following the 2000-m-depth isobath being 932 km from Line A to Line B and 990 km from Line B to Line W, the delays between lines correspond to a range of propagation speeds of 138–839 m s^{-1} between Line A and Line B, and 128–675 m s^{-1} between Line B and Line W. One delay estimate from B2 to W1 implies a 2196 m s^{-1} speed. Apart from this last outstanding value, the speeds and most observed directions of propagation between arrays are consistent with expectations based on barotropic wave mode calculations using a two-dimensional model with realistic topographic profiles from this region conducted by O'Rourke (2009). She found the gravest mode wave speed in the range 170–220 m s^{-1} (highlighted by shading in Fig. 11), corresponding to a barotropic Kelvin wave mode of length scale of order 2000 km perpendicular to the coast, therefore almost

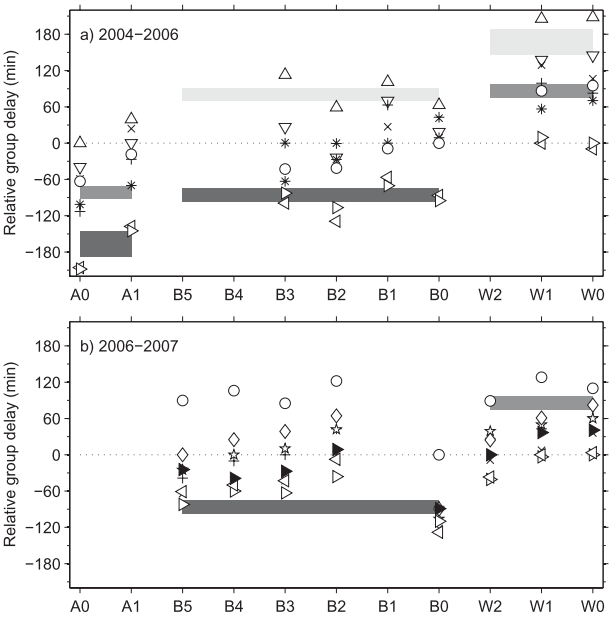

FIG. 11. Relative delay estimates between BPR record pairs for the time period (a) May 2004 to April 2006 and for (b) August 2006 to October 2007. Because these are relative delays for all pairs, values are plotted twice with opposite signs. The same symbols are used in both panels when appropriate to denote the delays estimated with respect to A0 (up pointing triangles), A1 (down pointing triangles), B0 (circles), B1 (asterisks), B2 (×'scrisscrosses), B3 (pluses), B4 (stars), B5 (diamonds), W0 (right pointing triangles), W1 (left pointing triangles), and W2 (black triangles). The boxes shaded light gray indicate a relative delay from Line A to lines B and W corresponding to a 170–220 m s^{-1} expected range of speeds. The boxes shaded medium gray indicate relative delays from Line B to lines A and W for the same speeds, and the boxes shaded dark gray from Line W to lines B and A. As an example in (a), it is estimated that a signal propagates from A0 to A1 in 40 min, from A0 to B0 in 63 min, from A0 to B1 in 101 min etc.

independent of depth over the continental slope, as observed here (since lags within each array are relatively small except lags calculated from B0 in 2006–07, which are clearly anomalous). Similar in-phase bottom pressure perturbations were observed from the Mid-Ocean Dynamics Experiment (MODE) bottom experiment between sites hundreds of kilometers apart near 28°N in the North Atlantic (Brown et al. 1975). These coherent, barotropic signals may also be responsible for the coherent sea level signals seen in satellite altimetry on the global continental slope (Hughes and Meredith 2006).

Assuming no variability on the eastern boundary, depth-independent pressure fluctuations on the western boundary would, from (1) be associated with a net meridional geostrophic flow across the latitude of the observations. At the latitude of lines A and B, a pressure anomaly p'_W of 1 mbar would produce a transport anomaly $Hp'_W/\rho f$ of 5 Sv assuming a depth $H = 5000$ m.

With a typical standard deviation of 2.5 mbar in the observations, this produces 12.5 Sv standard deviation in the transports. The rapid propagation speeds estimated here imply that these perturbations are transmitted along the continental slope between 38° and 43°N almost instantaneously (in a matter of hours) compared to their time scale (2.5 days, as estimated from the first spectral moment of a typical BPR record from Fig. 4a). It is likely that these adjustments are actually balanced rapidly by very similar pressure perturbations on the eastern boundary at the same latitudes but we have no way of assessing this. Such compensation was actually observed by Bryden et al. (2009) in boundary pressure records across 26°N in the Atlantic Ocean. If this also occurs at our latitudes, any net northward transports associated with these barotropic pressure perturbations are likely to be smaller than the 12.5 Sv number estimated above when the eastern boundary is constant. Nevertheless, these perturbations still produce net meridional transports across latitudes, on synoptic atmospheric time scales associated with global oscillations of masses between ocean basins (Stepanov and Hughes 2006). Detection of these signals, and their spatial coherence over large distances, demonstrates that the instruments are producing good quality data and are capable of detecting propagating signals. Their relevance for overturning processes, however, is small. Thus, we turn to the analysis of the layer transport time series derived from the pressure gradients, which are directly linked theoretically to the overturning processes by (2).

b. *Pressure gradient time series: Waves or advection?*

The two time series of integrated pressure gradients T_B and T_W overlap for 1325 days (Fig. 12). They are correlated at 0.18 with a p value associated with the test statistic of Ebisuzaki (1997) equal to 0.0046. The correlation after 30-day low-pass filtering of the time series is larger, at 0.32, with a p value of 0.0018. These significant levels of correlation are a validation of our methods, and an indication that the pressure gradients reconstructed at Line W and at Line B both capture a common signal which is large-scale. Such boundary signals were also found in OGCMs where they were related to overturning transport processes, in agreement with (2) (Roussenov et al. 2008; Bingham and Hughes 2008).

The variability of T_B and T_W and their covariability as a function of frequency is examined by a cross spectral analysis summarized in Fig. 13. The multitaper method used (see appendix) allows us to obtain spectral estimates at the period corresponding to the common length of the time series. Between periods of about 11 days and

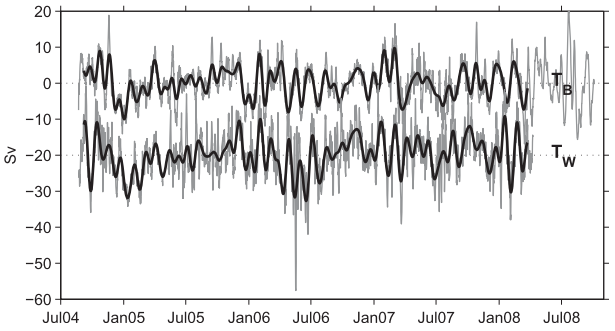

FIG. 12. The T_B and T_W time series at 12-h intervals (gray lines). Both time series are anomalies with 0 mean but T_W is offset by −20 Sv for legibility. The thick black curves are the 30-day low-passed versions.

90 days, the spectra are very similar apart from a strong peak at Line W near 34 days (Fig. 13a). Topographic Rossby waves have been identified as the major source of variability over a range of periods from about 1 to 3 weeks, in deep current meter measurements along the WAVE array region (Rhines 1971; Thompson 1971; Thompson and Luyten 1976; Louis et al. 1982; Shaw and Csanady 1988; Hogg 2000) and are usually ascribed to radiation from eddies interacting with topography, so it is to be expected that part of the variability will be quite localized. The 34-day peak at Line W may be an example of this, although it is at longer period. The low power at Line B for periods longer than 6 months probably results from the removal of low frequency power when detrending the BPR data. The Line B spectrum is also noticeably quieter than Line W at periods shorter than about 9 days, in contrast to the currents near Line A (Hogg 2000), which show enhanced energy at periods around 4 days.

The covariance between T_B and T_W occurs predominantly at low frequencies: at periods shorter than 10 days approximately, the power of the cross spectrum has decreased by two orders of magnitude compared to the low frequencies, and the coherence squared is generally low (Fig. 13b). The time scales where the coherence squared is significant seem limited to periods longer than approximately 85 days, reaching values greater than 0.5. At these time scales the phase estimates are near zero with no obvious dependence on frequency (Fig. 13c). Relatively high coherence squared also appears over the range between periods of about 30 and 80 days.

To investigate two possible causes of the correlation and coherence of the two time series, namely advection by the DWBC or propagation of boundary waves, we seek to determine plausible time delays between the two time series. First, a straightforward lagged cross correlation between the two time series peaks at 9 days with

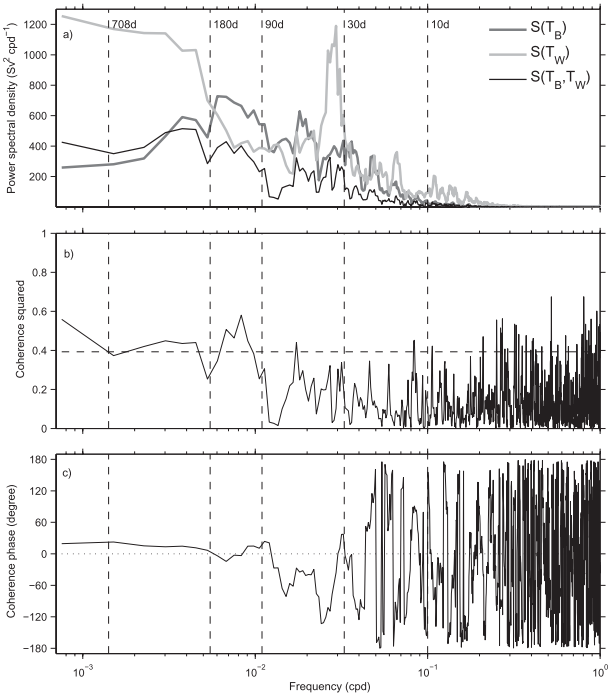

FIG. 13. Spectral analysis between T_B and T_W using a 7 Slepian tapers spectral estimate (Percival and Walden 1993). (a) Autospectral power density functions for T_B and T_W, and cross-spectral density function between the two. The upper and lower limits of the formal 95% confidence intervals (based on the χ^2 probability distribution function with 7×2 degrees of freedom) can be obtained by multiplying the curves by 0.5 and 2.5 approximately for each frequency value (these are not drawn for the legibility of the plot). (b) Coherence squared and (c) coherence phase. The vertical dashed lines in all panels indicate the frequency limits which define the ranges in which the time delay estimations are conducted. A negative slope of the phase with frequency in (c) indicates a possible propagation of a signal from Line B to Line W.

T_B leading T_W. However, as the spectral and cross spectral analyses showed, we can think of these time series as an aggregation of processes operating at different scales, and that the delay between processes may depend on the frequency. Hence, aggregating across all frequencies will produce an average delay that will exhibit biases for most frequencies. As such, we estimate constant time delays for specific frequency ranges, or group delays. Based on the cross-spectral analysis and dynamical considerations, we select the following five frequency limits, which define four distinct frequency ranges of estimation and six additional combined ranges. The first limit is $1/708$ cpd, which corresponds to the longest single deployment of BPRs at Line B. The second limit is $1/180$ cpd, which is an approximate upper limit for the frequencies that are affected by BPR drift corrections (not shown), as well as a change in power of the T_W spectrum. The third limit is $1/90$ cpd as it corresponds to a significant drop in the spectrum of T_B, as well as in the cross-spectrum and coherence squared and an apparent change of behavior of the coherence phase. The fourth limit is $1/30$ cpd because it marks another change in the phase behavior and is past the very large peak centered at $1/34$ cpd in the T_W spectrum. The fifth and final limit is $1/10$ cpd, because above this frequency ageostrophic variability in pressure may become more important as was shown by the pressure reconstruction (Fig. 6). Additionally, both cross spectrum and autospectra become dramatically reduced, making our model of constant group delay at these frequencies more vulnerable to biases in the estimation method.

The group delays in the frequency ranges defined by these limits are listed in Fig. 14 with 95% confidence intervals, where negative values denote a signal propagation from Line B to Line W. All estimates that include the $1/90$–$1/30$ cpd range have nominal negative delays between -10 and -12 days. The estimate in the $1/90$–$1/30$ cpd range itself is -11 days but the error bar is 46 days. The estimate in the $1/30$–$1/10$ cpd range is -19 days but the error bar is as large as the estimate itself. In contrast, the delay estimates at periods greater than 90 days are all clearly indistinguishable from zero, meaning that at these longer time scales the two time series are essentially coincident in time. Interestingly, the nominal delays in the individual ranges $1/708$–$1/80$ cpd and $1/180$–$1/90$ cpd are both positive, yet statistically indistinguishable from zero.

All the calculated delays that are significantly different from zero are negative, between -10 and -12 days, representing propagation from Line B to Line W as expected for CTWs. This corresponds to speeds of between 0.95 and 1.15 m s^{-1}, although the wide error bars imply speeds between about half and four times these values.

The most natural CTW mode to compare with is mode 1 (Fig. 2) because this mode has the same monotonic structure of bottom pressure as a function of depth as that seen in the observations. Yet, this mode has a propagation speed of over 5 m s^{-1}, which is significantly faster than that deduced from observations. The calculated wave speeds are both group and phase speeds, as the modes are calculated in the nondispersive, long-wave limit appropriate to periods of tens of days or longer. Higher modes have lower speeds, but even mode 3 propagates at almost 1.5 m s^{-1} and has an oscillatory structure in bottom pressure.

Thus we see that, while the signal propagation speeds are roughly similar in size to expected wave speeds, they do seem to be significantly slower. This situation is reminiscent of that discussed by Hallberg and Rhines (1996), in which forcing impinging on the continental slope sets up a ''topographic beta plume'' flow of counterpropagating jets on the slope. The flow develops along the path followed

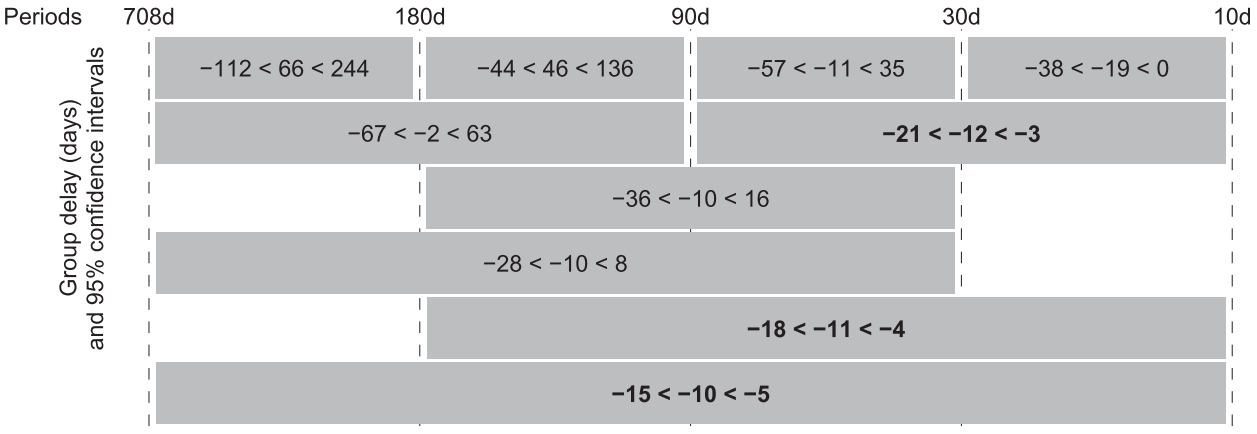

FIG. 14. Schematic of group delay estimates. These estimates are obtained for ranges of frequencies corresponding to the periods indicated at the top, also indicated in Fig. 13. Confidence intervals are at the 95% level. Group delay estimates which are different from zero according to the confidence intervals are in bold.

by topographically influenced waves propagating in the same sense as CTWs away from the forcing region, but it continues to develop after the first waves have passed. While the waves are responsible for propagating information along the continental slope from the forcing region, the continuing development of the flow in the wake of the first waves may produce a slower propagation of the fully developed ''beta plume'' circulation.

In summary, we find significant coherence between Line B and Line W, for the depth-dependent pressure mode, which is expected to be associated with an overturning circulation. We also find evidence for propagation of signals in the sense of CTWs, with a best estimate for the speed of about 1 m s^{-1}. This appears to be rather slow for the expected CTW mode and may be indicative of the slower development of a topographically controlled circulation in the wake of propagating CTWs.

c. *Can the observed delays be explained by advective processes?*

An alternative source of correlation between the two sections is advection of density or potential vorticity anomalies in the DWBC. The speeds discussed in the previous section seem too large to be explained by such processes, but these speeds were only derived for a subset of frequency ranges; other frequencies permit a wider range of speeds. This raises the question of whether advective processes could be responsible for any of the observed coherence.

Limiting our attention to signals propagating from Line B to Line W (i.e., negative delays), the numbers in Fig. 14 show that the longest permitted delay is 112 days (corresponding to 10 cm s^{-1} propagation speed). This lies in the 180–708-day period band for which the Line B time series is least reliable. For all other bands, the longest permitted delay is 67 days (17 cm s^{-1}), and the longest excluding the less reliable periods longer than 180 days is a 57-day delay (20 cm s^{-1}).

Tracer studies in this region (Holzer et al. 2010; van Sebille et al. 2011; Peña-Molino et al. 2011) suggest mean advection speeds of 1–3 cm s^{-1}, much slower than our observations would imply. However, tracer studies produce an average over all routes, including the most direct route in the DWBC as well as slower interior pathways, and both routes have been observed (Bower et al. 2009, and references therein). Could there be a precursor advective signal which takes the fastest route, and accounts for some of our observed correlations? Certainly, near-bottom velocities in the region do approach the 10–20 cm s^{-1} speeds which are at the limit of acceptability in our data (e.g., Shay et al. 1995; Bower and Hunt 2000; Pickart and Watts 1990). We investigate this in more detail, using independent Lagrangian data, and Eulerian data from Line W.

1) LAGRANGIAN ASSESSMENT

First we consider 25 acoustically tracked Range and Fixing of Sound (RAFOS) floats released in the DWBC between the Grand Banks and Cape Hatteras in 1994 and 1995 for the Boundary Current Experiment (BOUNCE) experiment (Bower and Hunt 2000). The floats, drifting at pressure levels between 3000 and 3600 db (deep) or between 900 and 1500 db (shallow), showed mean advective rates equatorward at 2–5 cm s^{-1} along the western boundary. Nine of the deep floats (Fig. 15a) crossed perpendicularly first Line B and then Line W, all with advective times longer than 57 days. Of these floats, two (b262 and b280) traveled the distance in 94 and 96 days, which is shorter than the 112-day limit diagnosed earlier for the 708-day to 6-month band of periods. The

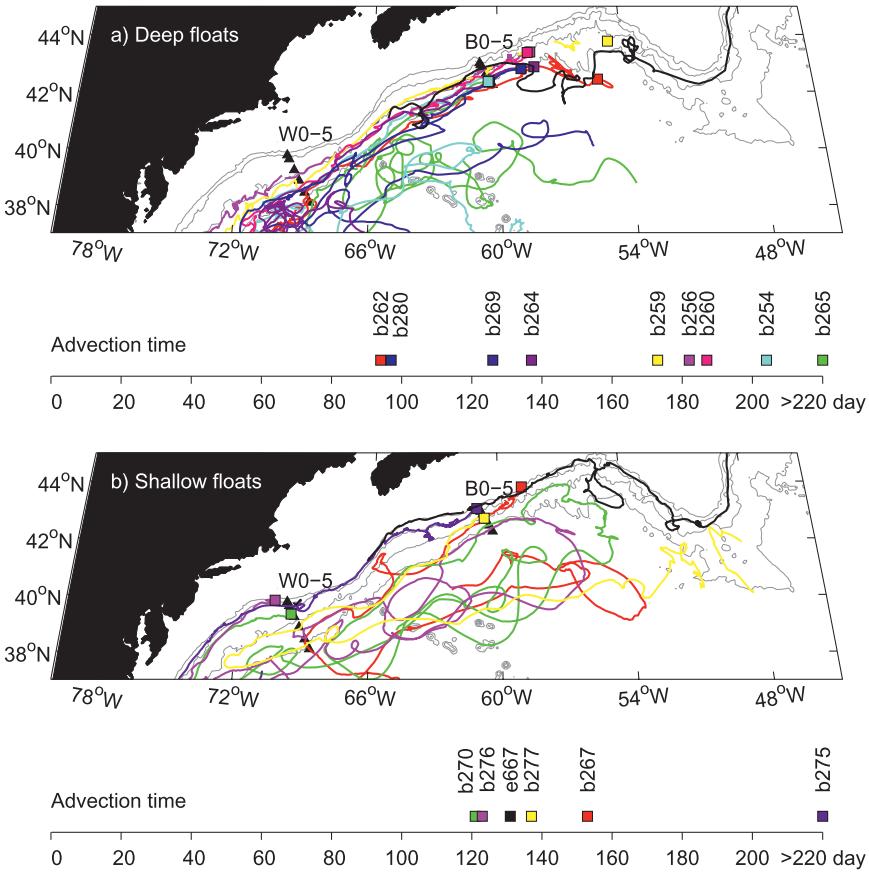

FIG. 15. (a) Trajectories of deep RAFOS floats from the BOUNCE experiment that crossed perpendicularly both Line B and Line W (colored trajectories and square symbols at the launching locations) and one deep float from the ExPath experiment (black trajectory). The launching position of the ExPath float is outside of the map. The 1-, 2-, 3-, and 4-km isobaths are contoured in gray. The locations of Line B and Line W moorings are indicated by black triangles. The corresponding advection times in days are reported on the horizontal scale below the map. (b) As in (a), but for shallow floats of BOUNCE and one shallow float from ExPath that flowed in this region (black trajectory) but its launching position is outside of this region.

slowest deep float (b265) took 480 days but this occurred because it recirculated before being recaptured by the DWBC. Three shallow floats were released upstream or very close to Line B and drifted eventually past Line W (Fig. 15b). Two other shallow floats were released downstream or near Line W but were advected first northeast by the Gulf Stream before being recaptured by the DWBC, eventually crossing Line B and Line W. The advection times for these shallow floats varied from 121 days to 512 days, all longer than the 57-, 67-, or even 112-day limits.

One may ask if the strength or the structure of the DWBC during BOUNCE was representative of the strength of the DWBC during our time series of pressure gradient. As such we also consider the 76 RAFOS floats from the ExPath experiment, which were released in the DWBC near 50°N between 2003 and 2006 at 700- and 1500-m depth (Bower et al. 2009). These floats tracking the recently ventilated Labrador Sea Water entered the subtropics via the interior of the gyre, not the DWBC. Only two floats, one shallow and one deep, were advected past Line B within the DWBC (Figs. 15a,b and see also Fig. 1 in Bower et al. 2009). The shallow float e667 crossed Line B around 16 October 2006 and reached approximately Line W 129 days later on 24 February 2007, mostly following the 1000-m isobath. The deep float e442 passed Line B around 20 July 2007, and reached approximately middistance between Line B and Line W in about 99 days, following for the most part the 3000-m isobath. The advection times from these two more recent floats are therefore consistent with the ones deduced from the earlier BOUNCE floats.

In conclusion no float from the BOUNCE or ExPath experiments traveled in the 57 days necessary to be within the error bars of observed delays at periods

shorter than 180 days. However, the negative 112-day limit of the confidence intervals for the delay estimate including time scales longer than 6 months is longer than the advective propagation times diagnosed from two BOUNCE floats. This overall suggests that advection by the DWBC could play a small role for the coherence on time scales longer than 6 months, but not on shorter time scales.

2) EULERIAN ASSESSMENT

The limited number of Lagrangian floats available for study may not capture the fastest possible advective route between lines B and W, but we can use Eulerian velocities to estimate propagation times without the complication of possible detrainment from the DWBC. Therefore, we consider the near-bottom along-slope velocity records from Line W, which were actually used to derive T_W (Fig. 5a). In fact it is near the bottom within the DWBC that the largest southwestward mean velocities are found at Line W (see Figs. 2 and 3 of Toole et al. 2011), so these velocity records are the most favorable to produce a fast signal propagation. We assume that these records are representative of the along-slope velocity on the continental slope between Line B and Line W. While this is unrealistic, it is the fastest signal propagation scenario that neglects recirculation and meanders of the DWBC, which are expected to lengthen the advection time. The velocity time series from the beginning of the overlap period of T_W and T_B are integrated in time until the cumulative distance equals 990 km, and this is repeated with a start time every subsequent day. This is equivalent to seeding particles at Line B every day in a DWBC with the velocity measured at Line W, along 6 isobaths ranging from 1000 to about 4000 m.

The results are displayed as histograms of advection times in Fig. 16. The median values of those histograms range from 147 to 367 days. These fall outside the 95% confidence intervals of the group delays of Fig. 14. However, advection times as short as 92 days occur from the near-bottom velocity at mooring W4. The value −92 is within the 95% confidence interval of the group delay estimate for the 708-day to 6-month band of periods. Yet, if one notes that the left limit of this interval (−112) is at 2.5% of the associated cumulative distribution function of the probability of the estimate, then −92 is still only at the 4.1% mark. In other words, there is only a 4.1% probability that the true delay is equal or less than −92 days. A 92-day propagation implies a mean advection speed greater than 0.12 m s^{-1}. This appears to be a period of relatively vigorous mean flow compared to other measurements of near-bottom velocities in this region. At the RAPID–Scotian Line (Hughes et al. 2013), the successor to Line B deployed in 2008, near-bottom records showed along-slope currents with extremes in the range 0.13–0.32 m s^{-1} depending on locations on the slope, yet the one-year-average along-slope current was in the range 0.01–0.05 m s^{-1}. Others such as Shay et al. (1995) reported extremes of velocity near 0.40 m s^{-1} at 3500-m depth on moorings of the Synoptic Ocean Prediction Experiment (SYNOP) in the vicinity of Line W, yet the mean for 26 months was only 0.07 m s^{-1} toward the southwest. Line W records at W4 indicated also extremes at 0.39 cm s^{-1}.

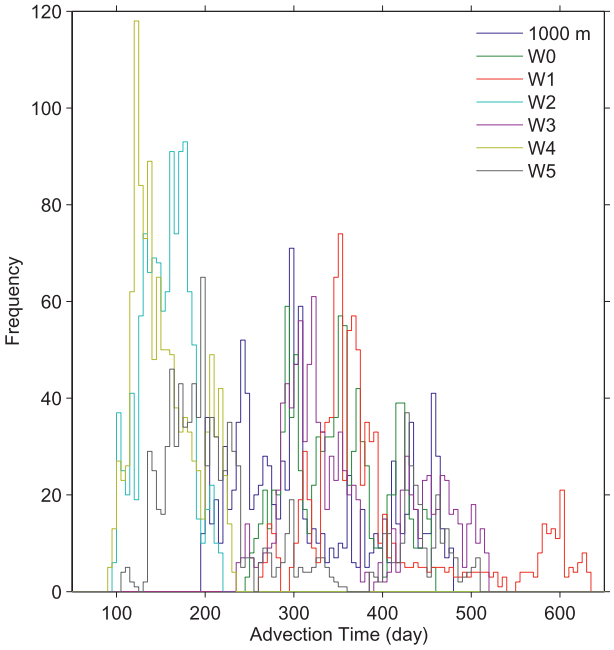

FIG. 16. Distribution of advection time scales between Line W and Line B based on integrating the velocity time series shown in Fig. 5a.

In conclusion, the analysis of Lagrangian and Eulerian velocity datasets suggests that that advection in the DWBC is too slow to account for the coherence at time scales shorter than six months. At longer periods advection cannot be excluded as a factor, but appears to be unlikely to account for the coherent signals seen here. We would expect advection in the DWBC or via diffusive pathways to play an increasing role at multiyear to decadal time scales (e.g., van Sebille et al. 2011; Peña-Molino et al. 2011; Holzer et al. 2010).

6. Summary and concluding remarks

Observations of bottom pressures collected between 2004 and 2008 as part of RAPID WAVE on the western boundary of the North Atlantic were analyzed. This

analysis included using boundary pressure gradient observations integrated to yield time series of western boundary contribution to basin-wide zonally integrated meridional transports, an approach shown to be successful in an OGCM (Bingham and Hughes 2008), to test the hypothesis that transport anomalies are communicated along the western boundary of the North Atlantic.

First, the analysis of detided BPR pressure records revealed the existence of signals propagating at speed of at least 128 m s^{-1} from northeast to southwest, in the general orientation of the axis formed by lines A, B, and W along the western boundary slope between approximately 43° and 38°N. These signals were attributed to near-barotropic coastally trapped waves propagating basin-scale disturbances excited by atmospheric forcing or oscillation of mass between ocean basins. Yet, these pressure oscillations were observed to be relatively independent of depth and are of little relevance for meridional overturning processes.

Second, the analysis of the covariance at time scales shorter than 3 months of the two time series of western boundary contribution to meridional transports suggested that pressure gradient signals propagate from Line B to Line W in between 3 and 21 days. The nominal delay of propagation is on average 11 days, which corresponds to a propagation speed of about 1 m s^{-1}. Such speed is roughly consistent with CTW speeds, but seems rather slow when compared with the realistic topography study of O'Rourke (2009).

Additionally, the two transport time series are significantly coherent for time scales longer than three months and nearly in phase. The examination of acoustically tracked float trajectories and Eulerian velocity records at Line W showed that the DWBC is too slow to propagate anomalies that could account for the observed coherence phase on time scales between three and six months. There is a small chance that advection in the DWBC could account for the observed coherence phase on longer time scales, but the advective mechanism seems most relevant at time scales longer than those amenable to analysis in our dataset.

The separate investigations of coherence by advection of the DWBC on one hand and the propagation of long wavelength CTW on the other hand may be a simplistic approach. Indeed, the investigations of O'Rourke (2009) neglected the possible influence of the mean flow on wave propagation, namely here the DWBC and the surface-intensified Gulf Stream, which could act to speed up or slow down the wave speeds. Many observations within the DWBC in this region provide evidence for the superposition, if not the interactions, of waves and DWBC flows. A velocity section taken during the BOUNCE experiment near our Line B showed a banded structure that was associated with TRW (Bower and Hunt 2000). The section of mean velocity at Line W reported by Toole et al. (2011) also showed such a banded structure. Near 35°N on the western boundary, Pickart and Watts (1990) found it necessary to extract a dominant part of the variance in velocity signals associated with waves, to quantify the underlying low-frequency DWBC fluctuations. Finally the waves themselves could be responsible for setting up the DWBC in the manner described by Hallberg and Rhines (1996) using an idealized 2-layer model. In this model, convectively-driven forcing leads to a ''topographic beta plume'' response in the form of currents and pressure changes, which form in the wake of TRWs as they propagate along the sloping western boundary away from the forcing region. Development of the currents behind the TRW could also account for the relatively slow propagation speeds found here.

While it is clear that the correlations we observe do not result from advective processes, the simple explanation in terms of CTW does not seem to be entirely satisfactory either, as the wave speed does not match expectations. Further investigations using high-resolution numerical modeling would help to disentangle the correlated signal from the various localized effects, which might also be expected in this region. Such effects are evident in the different levels found in the power spectra of T_W and T_B near 34 days time scale in Fig. 13a. Line W seems to capture much more variance associated with what is usually recognized to be TRWs activity in this region, traditionally attributed to wave radiation from the Gulf Stream and its rings (e.g., Pickart 1995).

This present study has not explored another possible source of coherence between the two transport time series which is that the correlation and coherence result from spatial correlation in an external forcing such as atmospheric pressure or wind stress. This will be investigated elsewhere.

Acknowledgments. This work was funded by the U.K. Natural Environment Research Council. Sofia Olhede was supported by EPSRC Grant EP/I005250/1. Initial observations at Station W (2001–04) were made possible by a grant from the G. Unger Vetlesen Foundation and support from the Woods Hole Oceanographic Institution. Since 2004, the Line W program has been supported by the U.S. National Science Foundation with supplemental contribution from WHOIs Ocean and Climate Change Institute. The authors thank Amy Bower for providing the BOUNCE and ExPath float data, which made an extremely valuable contribution to this study. The authors thank Miguel Angel Morales Maqueda for

assistance with the deployment and recovery of the data. We thank Eleanor O'Rourke for the use of her Ph.D. dissertation results and the adaptation of her figure for Fig. 2. Comments by Eleanor Frajka-Williams and Richard Williams improved the final manuscript. We thank Peter Rhines and an anonymous reviewer for their useful suggestions which improved the final manuscript.

APPENDIX

Spectral Methods

a. Spectral estimation

Cross-spectral density functions between random variables $x(n)$ and $y(n)$ with zero means are estimated using multitaper estimates (Percival and Walden 1993)

$$\hat{S}_{xy}(\nu) \equiv \frac{1}{K}\sum_{k=1}^{K}\hat{S}^k_{xy}(\nu) \quad \text{with} \tag{A1}$$

$$\hat{S}^k_{xy} \equiv \Delta t\left[\sum_{n=1}^{N} h^k(n)x(n)e^{-i2\pi\nu n\Delta t}\right]^* \times\left[\sum_{n=1}^{N} h^k(n)y(n)e^{-i2\pi\nu n\Delta t}\right], \tag{A2}$$

where ν is frequency, $(\cdot)^*$ designates the complex conjugate, N is the number of points in the time series, and $h^k(n)$, $n = 1, 2, \ldots, N$ is the kth discrete prolate spheroidal sequence with half time-bandwidth parameter NW and order $k = 1, \ldots, K$. To obtain smooth estimates, here NW = 4 and $K = 2\text{NW} - 1$ are chosen. Coherence squared and coherence phase estimates are computed as

$$\frac{|\hat{S}_{xy}|^2(\nu)}{\hat{S}_{xx}(\nu)\hat{S}_{yy}(\nu)}, \quad \arg[\hat{S}_{xy}(\nu)]. \tag{A3}$$

b. Group or time delay estimation

If a signal $x(t)$ is captured with a constant delay D as $y(t - D)$ then the theoretical cross spectrum between them is $S_{xy}(\nu) = S_{xx}(\nu)e^{-i2\pi\nu D}$, and the phase of the cross spectrum is a linear function of frequency. The group delay estimation method of Hannan and Thomson (1973) consists of implementing a method to obtain an estimate of D based on this expectation of the cross-spectrum.

An estimate $\hat{S}_{xy}(\nu)$ of the true cross spectrum can be written as

$$\hat{S}_{xy}(\nu) = |\hat{S}_{xy}(\nu)|e^{i\hat{\theta}(\nu)}, \tag{A4}$$

where $\hat{\theta}(\nu)$ is the cross-spectrum phase or coherence phase. Next, a band of frequencies B that contains M fundamental frequencies $1/(N\Delta t)$ is chosen, and the following quantity is computed

$$\hat{p}(D) = \frac{1}{M}\sum_{m=1}^{M}\hat{S}^1_{xy}(\nu_m)e^{-i2\pi\nu_m D} \tag{A5}$$

$$= \frac{1}{M}\sum_{m=1}^{M}|\hat{S}^1_{xy}(\nu_m)|e^{i[\theta(\nu_m)-2\pi\nu_m D]}, \quad \nu_m \in B \tag{A6}$$

where only one taper (the first prolate spheroidal sequence) is used to form the cross spectral estimate $\hat{S}^1_{xy}(\nu_m)$. No more smoothing of the cross spectral estimate is required as the frequency smoothing operation is done by the choice of the band B. Here, D is assumed to be a constant delay in the frequency band B and an estimate is produced for each B. The group delay estimate $\hat{D}$ is the value which maximizes $\hat{q}(D) = |\hat{p}(D)|^2$, which is found by a standard minimization routine on $-\hat{q}$.

Once $\hat{D}$ is obtained, uncertainties in the estimates are computed by considering the estimated maximized coherence squared in band B

$$\hat{\sigma}^2_B = \frac{q(\hat{D})}{\hat{S}^1_{xx}\hat{S}^1_{yy}}, \tag{A7}$$

which can be used to substitute for the true σ^2_B in the following expression for the variance of $\hat{D}$:

$$\text{Var}(\hat{D}) = \frac{3N^2}{M^3}\frac{1-\sigma^2_B}{2\pi\sigma^2_B}. \tag{A8}$$

Note that (A7) corrects the typographic error in Eq. (4) of Hannan and Thomson (1973), which has a square root for the denominator. Expression (A8) with (A7) is used to derive 95% confidence intervals assuming a normal distribution of the estimates:

$$\hat{D} \pm 1.96\left(\frac{3N^2}{M^3}\frac{1-\hat{\sigma}^2_B}{2\pi\hat{\sigma}^2_B}\right)^{1/2}. \tag{A9}$$

Note that (A8) indicates that $\text{Var}(\hat{D})$ increases with the length N of the time series but decreases with the width

of B. However, choosing a width too large for B may introduce biases by including frequencies bands where a constant group delay may not be a good model for the data.

REFERENCES

Bingham, R., and C. Hughes, 2008: Determining North Atlantic meridional transport variability from pressure on the western boundary: A model investigation. *J. Geophys. Res.,* **113,** C09008, doi:10.1029/2007JC004679.

——, ——, V. Roussenov, and R. Williams, 2007: Meridional coherence of the North Atlantic meridional overturning circulation. *Geophys. Res. Lett.,* **34,** L23606, doi:10.1029/2007GL031731.

Bower, A., and H. Hunt, 2000: Lagrangian observations of the deep western boundary current in the North Atlantic Ocean. Part I: Large-scale pathways and spreading rates. *J. Phys. Oceanogr.,* **30,** 764–783.

——, M. Lozier, S. Gary, and C. Böning, 2009: Interior pathways of the North Atlantic meridional overturning circulation. *Nature,* **459,** 243–247.

Brink, K., and D. Chapman, 1985: Programs for computing properties of coastal trapped waves and wind-driven motions over the continental shelf and slope. Woods Hole Oceanographic Institution Tech. Rep. WHOI-85-17, 45 pp.

British Oceanography Data Centre, cited 2003: *Centenary Edition of the GEBCO Digital Atlas.* Intergovernmental Oceanographic Commission and the International Hydrographic Organization. [Available online at http://www.gebco.net/data_and_products/gebco_digital_atlas/.]

Brown, W., W. Munk, F. Snodgrass, H. Mofjeld, and B. Zetler, 1975: MODE bottom experiment. *J. Phys. Oceanogr.,* **5,** 75–85.

Bryden, H., A. Mujahid, S. Cunningham, and T. Kanzow, 2009: Adjustment of the basin-scale circulation at 26°N to variations in Gulf Stream, deep western boundary current and Ekman transports as observed by the RAPID array. *Ocean Sci.,* **5,** 421–433.

Chelton, D., R. Deszoeke, M. Schlax, K. El Naggar, and N. Siwertz, 1998: Geographical variability of the first baroclinic Rossby radius of deformation. *J. Phys. Oceanogr.,* **28,** 433–460.

Chidichimo, M., T. Kanzow, S. Cunningham, W. Johns, and J. Marotzke, 2010: The contribution of eastern-boundary density variations to the Atlantic meridional overturning circulation at 26.5°N. *Ocean Sci.,* **6,** 475–490.

Cunningham, S., and Coauthors, 2007: Temporal variability of the Atlantic meridional overturning circulation at 26.5°N. *Science,* **317,** 935.

Ebisuzaki, W., 1997: A method to estimate the statistical significance of a correlation when the data are serially correlated. *J. Climate,* **10,** 2147–2153.

Hallberg, R., and P. Rhines, 1996: Buoyancy-driven circulation in an ocean basin with isopycnals intersecting the sloping boundary. *J. Phys. Oceanogr.,* **26,** 913–940.

Hannan, E., and P. Thomson, 1973: Estimating group delay. *Biometrika,* **60,** 241.

Hogg, N. G., 2000: Low-frequency variability on the western flanks of the Grand Banks. *J. Mar. Res.,* **58,** 523–545.

Holzer, M., F. Primeau, W. Smethie Jr., and S. Khatiwala, 2010: Where and how long ago was water in the western North Atlantic ventilated? Maximum entropy inversions of bottle data from WOCE line A20. *J. Geophys. Res.,* **115,** C07005, doi:10.1029/2009JC005750.

Hughes, C. W., and M. Meredith, 2006: Coherent sea-level fluctuations along the global continental slope. *Philos. Trans. Roy. Soc.,* **A364,** 885–901.

——, S. Elipot, M. A. Morales Maqueda, and J. Loder, 2013: Test of a method for monitoring the geostrophic meridional overturning circulation using only boundary measurements. *J. Atmos. Oceanic Technol.,* in press.

Huthnance, J., 1978: On coastal trapped waves: Analysis and numerical calculation by inverse iteration. *J. Phys. Oceanogr.,* **8,** 74–92.

Johnson, H., and D. Marshall, 2002: A theory for the surface Atlantic response to thermohaline variability. *J. Phys. Oceanogr.,* **32,** 1121–1132.

Kanzow, T., and Coauthors, 2010: Seasonal variability of the Atlantic meridional overturning circulation at 26.5°N. *J. Climate,* **23,** 5678–5698.

Louis, J., B. Petrie, and P. Smith, 1982: Observations of topographic rossby waves on the continental margin off Nova Scotia. *J. Phys. Oceanogr.,* **12,** 47–55.

Lozier, M., W. Owens, and R. Curry, 1995: The climatology of the North Atlantic. *Prog. Oceanogr.,* **36,** 1–44.

O'Rourke, E. A., 2009: The effect of topography on thermohaline adjustment. Ph.D. thesis, University of Liverpool, 191 pp.

Peña-Molino, B., T. Joyce, and J. Toole, 2011: Recent changes in the Labrador Sea Water within the Deep Western Boundary Current southeast of Cape Cod. *Deep-Sea Res. I,* **58,** 1019–1030, doi:10.1016/j.dsr.2011.07.006.

Percival, D. B., and A. T. Walden, 1993: *Spectral Analysis for Physical Applications.* Cambridge University Press, 612 pp.

Pickart, R., 1995: Gulf Stream-generated topographic Rossby waves. *J. Phys. Oceanogr.,* **25,** 574–586.

——, and D. Watts, 1990: Deep western boundary current variability at Cape Hatteras. *J. Mar. Res.,* **48,** 765–791.

Rhines, P., 1970: Edge-, bottom-, and Rossby waves in a rotating stratified fluid. *Geophys. Astrophys. Fluid Dyn.,* **1** (3–4), 273–302.

——, 1971: A note on long-period motions at Site D. *Deep-Sea Res.,* **18,** 21–26.

Roussenov, V., R. Williams, C. Hughes, and R. Bingham, 2008: Boundary wave communication of bottom pressure and overturning changes for the North Atlantic. *J. Geophys. Res.,* **113,** C08042, doi:10.1029/2007JC004501.

Shaw, P.-T., and G. T. Csanady, 1988: Topographic waves over the continental slope. *J. Phys. Oceanogr.,* **18,** 813–822.

Shay, T., J. Bane, D. Watts, and K. Tracey, 1995: Gulf Stream flow field and events near 68°W. *J. Geophys. Res.,* **100** (C11), 22 565–22 589.

Smith, W. H. F., and D. T. Sandwell, 1997: Global sea floor topography from satellite altimetry and ship depth soundings. *Science,* **277,** 1956–1962.

Stepanov, V., and C. Hughes, 2006: Propagation of signals in basin-scale ocean bottom pressure from a barotropic model. *J. Geophys. Res.,* **111,** C12002, doi:10.1029/2005JC003450.

Thompson, R., 1971: Topographic Rossby waves at a site north of the Gulf Stream. *Deep-Sea Res.,* **18,** 1–19.

——, and J. Luyten, 1976: Evidence for bottom-trapped topographic Rossby waves from single moorings. *Deep-Sea Res.,* **23,** 629–635.

Toole, J., R. Curry, T. Joyce, M. McCartney, and B. Penã Molino, 2011: Transport of the North Atlantic deep western boundary

current about 39°N, 70°W: 2004-2008. *Deep-Sea Res. II,* **58,** 1768–1780, doi:10.1016/j.dsr2.2010.10.058.

van Sebille, E., M. Baringer, W. Johns, C. Meinen, L. Beal, M. de Jong, and H. van Aken, 2011: Propagation pathways of classical Labrador Sea water from its source region to 26°N. *J. Geophys. Res.,* **116,** C12027, doi:10.1029/2011JC007171.

Wang, D., and C. Mooers, 1976: Coastal trapped waves in a continuously stratified ocean. *J. Phys. Oceanogr.,* **6,** 853–863.

Watts, D., and H. Kontoyiannis, 1990: Deep-ocean bottom pressure measurement: Drift removal and performance. *J. Atmos. Oceanic Technol.,* **7,** 296–306.

Wright, D., and Z. Xu, 2004: Double Kelvin waves over Newfoundland shelf-break. *Atmos.–Ocean,* **42,** 101–111.

Zhang, R., 2010: Latitudinal dependence of Atlantic meridional overturning circulation (AMOC) variations. *Geophys. Res. Lett.,* **37,** L16703, doi:10.1029/2010GL044474.